

Sixth order WENO schemes with Z-type nonlinear weighting procedure for nonlinear degenerate parabolic equations

Jiaxi Gu*, Samala Rathan†

Abstract

In this paper we develop new nonlinear weights of sixth order finite difference weighted essentially non-oscillatory (WENO) schemes for nonlinear degenerate parabolic equations. We construct two Z-type nonlinear weights: one is based on the L^2 norm and the other depends on the L^1 norm, yielding improved WENO schemes with more accurate resolution. We also confirm that the new devised nonlinear weights satisfy the sufficient conditions of sixth order accuracy. Finally, one- and two-dimensional numerical examples are presented to demonstrate the improved behavior of WENO schemes with new weighting procedure.

Keywords: Finite Difference, WENO scheme, Z-type nonlinear weights, Nonlinear degenerate parabolic equation.

AMS subject classification: 41A10, 65M06

1 Introduction

In this paper we are interested in solving the one-dimensional parabolic equation

$$u_t = b(u)_{xx}, \quad (1.1)$$

where $u = u(x, t)$ is a scalar quantity and $b'(u) \geq 0$.

One example of such nonlinear equation is the porous medium equation (PME) of the degenerate parabolic type,

$$u_t = (u^m)_{xx}, \quad m > 1, \quad (1.2)$$

which describes the flow of an isentropic gas through a porous medium [1, 16], the heat radiation in plasmas [23] and various physical processes. The classical linear heat equation can be considered to be the limit of PME (1.2) as $m \rightarrow 1$. Assuming $u \geq 0$, the PME could be written in the form

$$u_t = (mu^{m-1}u_x)_x.$$

Then the PME is parabolic only at those points where $u \neq 0$, while it degenerates as the vanishing of the term mu^{m-1} wherever $u = 0$. In other words, the PME is a degenerate parabolic equation. One important property of the PME is the finite propagation, which is different from the infinite speed of propagation in the classical heat equation. This property implies the appearance of free boundaries that separate the regions where the solution is positive from those where $u = 0$, giving rise to the sharp interfaces [21]. Since the free boundaries move with respect to time, their behavior looks similar to the behavior of shocks in the hyperbolic conservation laws. So it is reasonable to apply the ENO/WENO philosophy to the PME, enabling the free boundaries to be well resolved.

*Email: jiaxigu@postech.ac.kr, Department of Mathematics & POSTECH MINDS (Mathematical Institute for Data Science), Pohang University of Science and Technology, Pohang 37673, Korea

†Email: rathans.math@iipe.ac.in, Faculty of Mathematics, Department of Humanities and Sciences, Indian Institute of Petroleum and Energy-Visakhapatnam, 530003, India

In [15], Liu et al. constructed the finite difference WENO (WENO-LSZ) schemes for the equation (1.1), which approximate the second derivative term directly by a conservative flux difference. However, unlike the positive linear weights of WENO schemes for hyperbolic conservation laws [11, 19], the negative linear weights exist so that some special care, such as the technique in [18], was applied to guarantee the non-oscillatory performance in regions of sharp interfaces. Following the definition of the smoothness indicators in [11, 19] and invoking the mapped function in [9], the resulting nonlinear weights meet the requirement of sixth order accuracy. In [6], Hajipour and Malek proposed the modified WENO (MWENO) scheme with Z-type nonlinear weights [3] and nonstandard Runge–Kutta (NRK) schemes. Further, the hybrid scheme based on the spatial MWENO and the temporal NRK schemes was employed to solve the equation (1.1) numerically. Recently, Rathan et al. [17] proposed a new type of local and global smoothness indicators in L^1 norm based on the concept of achieving a higher order approximation to the lower order derivatives through undivided differences and subsequently constructed the new Z-type nonlinear weights, and Jiang [12] designed an alternative formulation to approximate the second derivatives in a conservative form, where the odd order derivatives at half points were used to construct the numerical flux.

In this paper we generalize both Z-type nonlinear weights in [6, 17] in two approaches. One is the extension of the MWENO nonlinear weights, which are based on the smoothness indicators in [15] of L^2 norms, to a more general Z-type nonlinear weights. The other is to design the novel Z-type nonlinear weights depending on new smoothness indicators with the notion of generalized undivided difference [8]. We take full advantage of the information about the derivatives of a flux function on a given substencil. In both cases, not only is the computational cost reduced without estimating the mapped function in WENO-LSZ, but the non-oscillatory performance is improved since there exist small-scale oscillations around the sharp interfaces for WENO-LSZ in some cases as the time advances whereas those oscillations are damped by our schemes. An analysis of nonlinear weights shows that the proposed WENO schemes satisfy the sufficient criteria for the sixth order accuracy. Also the implementation of WENO schemes for the equation (1.1) could be extended to the convection–diffusion equations with the WENO schemes for convection terms [3, 9, 11, 19] and to multi-space dimensions in a dimension-by-dimension approach.

The paper is organized as follows. In Section 2, the sixth order WENO-LSZ scheme for the parabolic equation (1.1) and some of the relevant analytical results are reviewed. Section 3 presents the Z-type nonlinear weights based on L^2 norms and generalized undivided differences, respectively. We also demonstrate that those nonlinear weights satisfies the sufficient conditions to achieve sixth order accuracy. In Section 4, the proposed schemes and the WENO-LSZ scheme are compared with the simulation of one- and two-dimensional numerical experiments. Section 4 contains numerical experiments, including 1D and 2D heat equations for the sixth order verification; 1D and 2D PME with various initial conditions; 1D and 2D Buckley–Leverett equations; 1D and 2D strongly degenerate parabolic convection-diffusion equations; 1D glacier hydrology model. A brief concluding remark is presented in Section 5.

2 WENO approximation to the second derivative

In this section, we review the direct WENO discretization to the second derivative in the conservation form [15]. Consider a uniform grid defined by the points $x_0 < x_1 < \dots < x_{N-1} < x_N$ with $x_{i\pm 1/2} = x_i \pm \Delta x/2$, $i = 0, \dots, N$, where $\Delta x = x_{i+1} - x_i$ is the uniform grid spacing. Then the spatial domain is discretized by this uniform grid. The semi-discrete form of Equation (1.1) with respect to t , yields

$$\frac{du_i(t)}{dt} = \frac{\partial^2 b}{\partial x^2} \bigg|_{x=x_i}, \quad (2.1)$$

where $u_i(t)$ is the numerical approximation to the point value $u(x_i, t)$. Define the function $h(x)$ implicitly by

$$b(u(x)) = \frac{1}{\Delta x^2} \int_{x-\Delta x/2}^{x+\Delta x/2} \left(\int_{\eta-\Delta x/2}^{\eta+\Delta x/2} h(\xi) d\xi \right) d\eta.$$

Differentiating both sides twice with respect to x , we obtain

$$b(u)_{xx} = \frac{h(x + \Delta x) - 2h(x) + h(x - \Delta x)}{\Delta x^2}.$$

Setting $g(x)$ as $g(x) = h(x + \Delta x/2) - h(x - \Delta x/2)$ gives the equation

$$\left. \frac{\partial^2 b}{\partial x^2} \right|_{x=x_i} = \frac{g_{i+1/2} - g_{i-1/2}}{\Delta x^2},$$

where $g_{i\pm 1/2} = g(x_{i\pm 1/2})$. Then the equation (2.1) becomes

$$\frac{du_i(t)}{dt} = \frac{g_{i+1/2} - g_{i-1/2}}{\Delta x^2}. \quad (2.2)$$

In order to approximate $g_{i+1/2}$, a polynomial approximation $q(x)$ to $h(x)$ of degree at most 5 is constructed on the 6-point stencil S^6 , as shown in Figure 1. The polynomial approximation

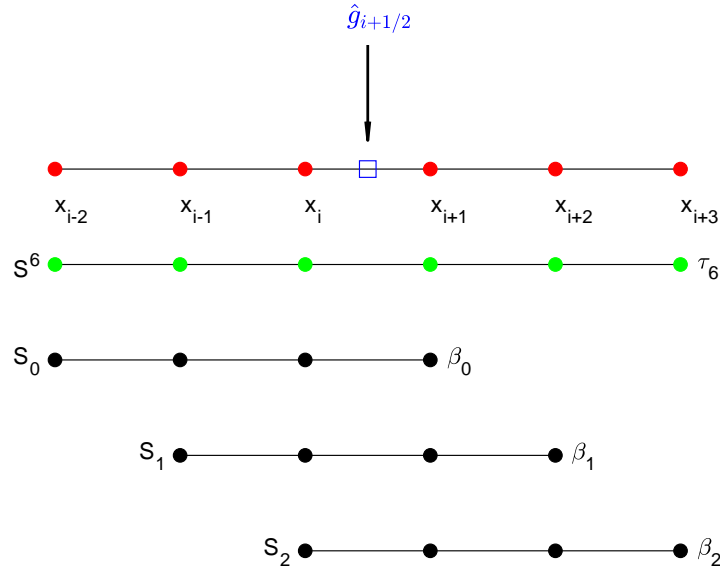


Figure 1: The numerical flux $\hat{g}_{i+1/2}$ is constructed on the stencil $S^6 = \{x_{i-2}, \dots, x_{i+3}\}$ with six uniform points, as well as three 4-point substencils S_0, S_1, S_2 .

$p(x)$ to $g(x)$ of degree at most 4 is obtained by taking the difference of $q(x + \Delta x/2)$ and $q(x - \Delta x/2)$,

$$g(x) = h(x + \Delta x/2) - h(x - \Delta x/2) \approx q(x + \Delta x/2) - q(x - \Delta x/2) = p(x).$$

Evaluating $p(x)$ at $x = x_{i+1/2}$ yields the finite difference numerical flux

$$\hat{g}_{i+1/2}^{\text{FD}} = p(x_{i+1/2}) = -\frac{1}{90}b_{i-2} + \frac{5}{36}b_{i-1} - \frac{49}{36}b_i + \frac{49}{36}b_{i+1} - \frac{5}{36}b_{i+2} + \frac{1}{90}b_{i+3}. \quad (2.3)$$

The numerical flux $\hat{g}_{i-1/2}^{\text{FD}}$ is obtained by shifting one grid to the left, which gives

$$\hat{g}_{i-1/2}^{\text{FD}} = -\frac{1}{90}b_{i-3} + \frac{5}{36}b_{i-2} - \frac{49}{36}b_{i-1} + \frac{49}{36}b_i - \frac{5}{36}b_{i+1} + \frac{1}{90}b_{i+2}. \quad (2.4)$$

Applying the Taylor expansions to $\hat{g}_{i\pm 1/2}^{\text{FD}}$ (2.3) and (2.4) would give

$$\hat{g}_{i+1/2}^{\text{FD}} = g_{i+1/2} + \frac{1}{560}h_i^{(7)}\Delta x^7 + O(\Delta x^8), \quad (2.5)$$

$$\hat{g}_{i-1/2}^{\text{FD}} = g_{i-1/2} + \frac{1}{560}h_i^{(7)}\Delta x^7 + O(\Delta x^8). \quad (2.6)$$

Replacing $g_{i\pm 1/2}$ in (2.2) by (2.5) and (2.6), respectively, we have the sixth order approximation

$$\frac{du_i(t)}{dt} = \frac{\hat{g}_{i+1/2}^{\text{FD}} - \hat{g}_{i-1/2}^{\text{FD}}}{\Delta x^2} + O(\Delta x^6).$$

A similar approach can be used to obtain a polynomial $p_k(x)$ of degree at most 2 on each 4-point subinterval $S_k = \{x_{i-2+k}, \dots, x_{i+1+k}\}$ with $k = 0, 1, 2$, resulting in the numerical flux $\hat{g}_{i+1/2}^k$,

$$\begin{aligned} \hat{g}_{i+1/2}^0 &= \frac{1}{12}b_{i-2} - \frac{1}{4}b_{i-1} - \frac{3}{4}b_i + \frac{11}{12}b_{i+1}, \\ \hat{g}_{i+1/2}^1 &= \frac{1}{12}b_{i-1} - \frac{5}{4}b_i + \frac{5}{4}b_{i+1} - \frac{1}{12}b_{i+2}, \\ \hat{g}_{i+1/2}^2 &= -\frac{11}{12}b_i + \frac{3}{4}b_{i+1} + \frac{1}{4}b_{i+2} - \frac{1}{12}b_{i+3}. \end{aligned} \quad (2.7)$$

It is clear that the linear combination of all $\hat{g}_{i+1/2}^k$ can produce $\hat{g}_{i+1/2}^{\text{FD}}$ that approximates the flux $g_{i+1/2}$ in (2.2), that is, there are linear weights $d_0 = d_2 = -\frac{2}{15}$ and $d_1 = \frac{19}{15}$ such that

$$\hat{g}_{i+1/2}^{\text{FD}} = \sum_{k=0}^2 d_k \hat{g}_{i+1/2}^k. \quad (2.8)$$

Similarly, an index shift by -1 returns the corresponding $\hat{g}_{i-1/2}^k$ and the relation between $\hat{g}_{i-1/2}^{\text{FD}}$ and $\hat{g}_{i-1/2}^k$.

Since (2.8) is not a convex combination of (2.7) as the linear weights d_0 and d_2 are negative, the WENO procedure cannot be applied directly to obtain a stable scheme. The test cases in [18] showed that WENO schemes without special treatment to the negative weights may lead to the blow-up of the numerical solution. Thus the splitting technique in [18] could be utilized to treat the negative weights d_0 and d_2 . The linear weights are split into two parts: positive and negative,

$$\tilde{\gamma}_k^+ = \frac{1}{2}(d_k + 3|d_k|), \quad \tilde{\gamma}_k^- = \tilde{\gamma}_k^+ - d_k, \quad k = 0, 1, 2.$$

Then $d_k = \tilde{\gamma}_k^+ - \tilde{\gamma}_k^-$ and

$$\begin{aligned} \tilde{\gamma}_0^+ &= \frac{2}{15}, \quad \tilde{\gamma}_1^+ = \frac{38}{15}, \quad \tilde{\gamma}_2^+ = \frac{2}{15}; \\ \tilde{\gamma}_0^- &= \frac{4}{15}, \quad \tilde{\gamma}_1^- = \frac{19}{15}, \quad \tilde{\gamma}_2^- = \frac{4}{15}. \end{aligned}$$

We scale them by

$$\sigma^\pm = \sum_{k=0}^2 \tilde{\gamma}_k^\pm, \quad \gamma_k^\pm = \tilde{\gamma}_k^\pm / \sigma^\pm, \quad k = 0, 1, 2.$$

Then the linear positive and negative weights γ_k^\pm are given by

$$\begin{aligned}\gamma_0^+ &= \frac{1}{21}, & \gamma_1^+ &= \frac{19}{21}, & \gamma_2^+ &= \frac{1}{21}; \\ \gamma_0^- &= \frac{4}{27}, & \gamma_1^- &= \frac{19}{27}, & \gamma_2^- &= \frac{4}{27},\end{aligned}\tag{2.9}$$

which satisfy

$$d_k = \sigma^+ \gamma_k^+ - \sigma^- \gamma_k^-. \tag{2.10}$$

Following the definition of the smoothness indicators in [11, 19], which measure the regularity of the polynomial approximation $p_k(x)$ over some interval, the smoothness indicators are defined as

$$\beta_k = \sum_{l=1}^2 \Delta x^{2l-1} \int_{x_i}^{x_{i+1}} \left(\frac{d^l}{dx^l} p_k(x) \right)^2 dx,$$

which gives

$$\begin{aligned}\beta_0 &= \frac{13}{12} (b_{i-2} - 3b_{i-1} + 3b_i - b_{i+1})^2 + \frac{1}{4} (b_{i-2} - 5b_{i-1} + 7b_i - 3b_{i+1})^2, \\ \beta_1 &= \frac{13}{12} (b_{i-1} - 3b_i + 3b_{i+1} - b_{i+2})^2 + \frac{1}{4} (b_{i-1} - b_i - b_{i+1} + b_{i+2})^2, \\ \beta_2 &= \frac{13}{12} (b_i - 3b_{i+1} + 3b_{i+2} - b_{i+3})^2 + \frac{1}{4} (-3b_i + 7b_{i+1} - 5b_{i+2} + b_{i+3})^2.\end{aligned}\tag{2.11}$$

The integration over the interval $[x_i, x_{i+1}]$ is performed to satisfy the symmetry property of the parabolic equation, and the factor Δx^{2l-1} is introduced to remove any Δx dependency in the derivatives. The nonlinear positive and negative weights ω_k^\pm are defined as

$$\omega_k^\pm = \frac{\alpha_k^\pm}{\sum_{l=0}^2 \alpha_l^\pm}, \quad \alpha_k^\pm = \frac{\gamma_k^\pm}{(\beta_k + \epsilon)^2}, \quad k = 0, 1, 2, \tag{2.12}$$

where $\epsilon = 10^{-6}$ in [15] avoids the denominator becoming zero. Based on the relation (2.10) for the linear weights, the nonlinear weights are defined by

$$\omega_k = \sigma^+ \omega_k^+ - \sigma^- \omega_k^-. \tag{2.13}$$

In [15], Liu et al. obtained the sufficient conditions to attain sixth order accuracy

$$\omega_0 - \omega_2 = O(\Delta x^4), \tag{2.14}$$

$$\omega_k - d_k = O(\Delta x^3). \tag{2.15}$$

However, the nonlinear weights defined in (2.12) and (2.13) gives

$$\omega_k - d_k = O(\Delta x),$$

where the condition (2.15) is not satisfied. To increase the accuracy of the nonlinear weights, the mapped function in [9] are introduced:

$$g_k(\omega) = \frac{\omega(d_k + d_k^2 - 3d_k\omega + \omega^2)}{d_k^2 + \omega(1 - 2d_k)}, \quad k = 0, 1, 2.$$

The mapped nonlinear weights are

$$\omega_k^M = \frac{\alpha_k}{\sum_{l=0}^2 \alpha_l}, \quad \alpha_k = g_k(\omega_k), \quad k = 0, 1, 2.$$

It can be shown with Taylor expansion that

$$\begin{aligned}\omega_0^M - \omega_2^M &= O(\Delta x^4), \\ \omega_k^M - d_k &= O(\Delta x^3).\end{aligned}$$

So both conditions (2.14) and (2.15) are satisfied. Hence the WENO numerical flux is

$$\hat{g}_{i+1/2} = \sum_{k=0}^2 \omega_k^M \hat{g}_{i+1/2}^k,$$

where $\hat{g}_{i+1/2}^k$, $k = 0, 1, 2$ are given by (2.7). Then the semi-discrete finite difference WENO scheme of the conservation form is

$$\frac{du_i(t)}{dt} = \frac{\hat{g}_{i+1/2} - \hat{g}_{i-1/2}}{\Delta x^2}.$$

Remark 2.1. A major difference between the WENO approximations to the first and second derivatives is that in one stencil, two numerical fluxes $\hat{f}_{i-1/2}^+$ and $\hat{f}_{i+1/2}^-$ at the respective points $x_{i-1/2}$ and $x_{i+1/2}$ need evaluating for the first derivative, while only one numerical flux $\hat{g}_{i+1/2}$ at $x_{i+1/2}$ is estimated for the second derivative.

3 Z-type nonlinear weights

The Z-type nonlinear weights were first proposed in 2007 by Borges et al. [3]. The global smoothness indicator is introduced to give higher order, which means that the lower order terms happen to cancel out if the function is smooth in the stencil. The free parameter p is important to increase the separation of scales, as well as control the amount of numerical dissipation. We will investigate the Z-type nonlinear weights for the numerical flux $\hat{g}_{i+1/2}$ in details in this section.

3.1 Generalization of MWENO weights

In [6], the global smoothness indicator τ_6 on the stencil S^6 is the absolute difference between β_0 and β_2 ,

$$\tau_6 = |\beta_0 - \beta_2|,$$

and the nonlinear positive and negative weights are defined as

$$\omega_k^\pm = \frac{\alpha_k^\pm}{\sum_{l=0}^2 \alpha_l^\pm}, \quad \alpha_k^\pm = \gamma_k^\pm \left(1 + \left(\frac{\tau_6}{\beta_k + \epsilon} \right)^2 \right), \quad k = 0, 1, 2,$$

with γ_k^\pm in (2.9) and $\epsilon = 10^{-30}$. We generalize those weights to

$$\omega_k^\pm = \frac{\alpha_k^\pm}{\sum_{l=0}^2 \alpha_l^\pm}, \quad \alpha_k^\pm = \gamma_k^\pm \left(C + \left(\frac{\tau_6}{\beta_k + \epsilon} \right)^p \right), \quad k = 0, 1, 2, \quad (3.1)$$

where $\epsilon = 10^{-40}$. As defined in (2.13), the nonlinear weights are

$$\omega_k = \sigma^+ \omega_k^+ - \sigma^- \omega_k^-.$$

Here the parameter C is introduced to increase the contribution of linear weights when the smoothness indicators have comparable magnitude [10]. The parameter p , which is independent of C , is the key to satisfying the sufficient conditions (2.14) and (2.15) for sixth order accuracy in smooth regions.

Expanding the smoothness indicators β_k (2.11) in Taylor series at $x = x_{i+1/2}$, we obtain

$$\begin{aligned}\beta_0 &= b_{i+1/2}''^2 \Delta x^4 + \left(\frac{13}{12} b_{i+1/2}'''^2 - \frac{7}{12} b_{i+1/2}'' b_{i+1/2}^{(4)} \right) \Delta x^6 + \left(-\frac{13}{6} b_{i+1/2}''' b_{i+1/2}^{(4)} + \frac{1}{2} b_{i+1/2}'' b_{i+1/2}^{(5)} \right) \Delta x^7 + O(\Delta x^8), \\ \beta_1 &= b_{i+1/2}''^2 \Delta x^4 + \left(\frac{13}{12} b_{i+1/2}'''^2 + \frac{5}{12} b_{i+1/2}'' b_{i+1/2}^{(4)} \right) \Delta x^6 + O(\Delta x^8), \\ \beta_2 &= b_{i+1/2}''^2 \Delta x^4 + \left(\frac{13}{12} b_{i+1/2}'''^2 - \frac{7}{12} b_{i+1/2}'' b_{i+1/2}^{(4)} \right) \Delta x^6 + \left(\frac{13}{6} b_{i+1/2}''' b_{i+1/2}^{(4)} - \frac{1}{2} b_{i+1/2}'' b_{i+1/2}^{(5)} \right) \Delta x^7 + O(\Delta x^8).\end{aligned}$$

If there is no inflection (or undulation) point at $x_{i+1/2}$, i.e., the second derivative is nonzero, then

$$\tau_6 = \left| \frac{13}{3} b_{i+1/2}''' b_{i+1/2}^{(4)} - b_{i+1/2}'' b_{i+1/2}^{(5)} \right| \Delta x^7 + O(\Delta x^8).$$

Since τ_6 is of order $O(\Delta x^7)$ and each β_k is of order $O(\Delta x^4)$, one can find that

$$\left(\frac{\tau_6}{\beta_k} \right)^p = O(\Delta x^{3p}),$$

by setting $\epsilon = 0$ in the Taylor expansion analysis. From the definitions (3.1),

$$\begin{aligned}\alpha_k^\pm &= \gamma_k^\pm \left(C + O(\Delta x^{3p}) \right), \\ \omega_k^\pm &= \gamma_k^\pm \left(1 + O(\Delta x^{3p}) \right).\end{aligned}$$

Thus the nonlinear weights (2.13) are given by

$$\omega_k = \sigma^+ \omega_k^+ - \sigma^- \omega_k^- = \sigma^+ \gamma_k^+ \left(1 + O(\Delta x^{3p}) \right) - \sigma^- \gamma_k^- \left(1 + O(\Delta x^{3p}) \right) = d_k + O(\Delta x^{3p}).$$

The minimum value p to satisfy both conditions (2.14) and (2.15) is $p = 4/3$.

Now we consider the convergence behavior of the nonlinear weights when there exists an inflection point at $x_{i+1/2}$, that is, the second derivative is zero but the third derivative is nonzero. Then it can be verified through the Taylor expansion analysis above that

$$\omega_k = d_k + O(\Delta x^p),$$

and it is clear that $p = 4$ is the minimum value to maintain the sixth order accuracy.

As pointed out by Borges et al. [3], increasing the value of p amplifies the numerical dissipation around the discontinuities. We then choose $p = 4/3$ in this paper even if it does not satisfy the sufficient conditions (2.14) and (2.15) at the inflection points. However, our numerical experiments show that it still provide the sixth order accuracy overall. As for the value of C , we set $C = 10$ after studying the different values of C for PME (1.2) (see Example 4.2 in Section 4).

3.2 New nonlinear weights based on generalized undivided differences

In [7, 8], the notion of the generalized undivided difference to higher order functionals was introduced so that it can be used to achieve a higher order approximation to the derivatives of a function than the classical undivided difference. We will apply the generalized undivided difference to the substencils S_k , $k = 0, 1, 2$, for the L^1 -norm smoothness indicators. Let \mathbb{I}_k be the index set for the substencil $S_k = \{x_{i+j} : j \in \mathbb{I}_k\}$. Then \mathbb{I}_k has a cardinality of 4. Since an interpolating polynomial of degree at most 3 can be derived on each substencil S_k , the generalized undivided difference of order ν up to 3 can be obtained as follows. Let A be a 4×4

matrix with entries $A_{ij} = (k - 3 + j - 1/2)^{i-1}/(i-1)!$ and $\Delta^{[\nu]}$ the column vector with each entry the Kronecker delta such that

$$A = \begin{bmatrix} 1 & 1 & 1 & 1 \\ k-5/2 & k-3/2 & k-1/2 & k+1/2 \\ (k-5/2)^2/2 & (k-3/2)^2/2 & (k-1/2)^2/2 & (k+1/2)^2/2 \\ (k-5/2)^3/6 & (k-3/2)^3/6 & (k-1/2)^3/6 & (k+1/2)^3/6 \end{bmatrix}, \quad \Delta^{[\nu]} = \begin{bmatrix} \delta_{\nu 0} \\ \delta_{\nu 1} \\ \delta_{\nu 2} \\ \delta_{\nu 3} \end{bmatrix}.$$

Since the matrix A is nonsingular, the coefficient vector

$$X_k^{[\nu]} = \left(\chi_{k(k-2)}^{[\nu]}, \chi_{k(k-1)}^{[\nu]}, \chi_{kk}^{[\nu]}, \chi_{k(k+1)}^{[\nu]} \right)^T$$

is given by $X_k^{[\nu]} = A^{-1} \Delta^{[\nu]}$. Then the generalized undivided difference of order ν on the sub-tencil S_k ($\nu = 1, 2, 3$, $k = 0, 1, 2$) is defined as

$$D_k^\nu b_{i+1/2} = \sum_{j \in \mathbb{I}_k} \chi_{kj}^{[\nu]} b(x_{i+j}).$$

Specifically,

$$\begin{aligned} D_k^1 b_{i+1/2} &= \left(\frac{1}{24} + \frac{k}{2} - \frac{k^2}{2} \right) b_{i-2+k} + \left(-\frac{1}{8} - \frac{5k}{2} + \frac{3k^2}{2} \right) b_{i-1+k} + \left(-\frac{7}{8} + \frac{7k}{2} - \frac{3k^2}{2} \right) b_{i+k} + \left(\frac{23}{24} - \frac{3k}{2} + \frac{k^2}{2} \right) b_{i+1+k}, \\ D_k^2 b_{i+1/2} &= \left(-\frac{1}{2} + k \right) b_{i-2+k} + \left(\frac{5}{2} - 3k \right) b_{i-1+k} + \left(-\frac{7}{2} + 3k \right) b_{i+k} + \left(\frac{3}{2} - k \right) b_{i+1+k}, \\ D_k^3 b_{i+1/2} &= -b_{i-2+k} + 3b_{i-1+k} - 3b_{i+k} + b_{i+1+k}. \end{aligned}$$

In [8], it is shown that

$$D_k^\nu b_{i+1/2} = \frac{d^\nu b}{dx^\nu}(x_{i+1/2}) \Delta x^\nu + O(\Delta x^4),$$

as can be verified with Taylor expansion. Unlike the smoothness indicators in [17] that only use $D_k^2 b_{i+1/2}$ and $D_k^3 b_{i+1/2}$, we take full advantage of the information in generalized undivided differences and define the new smoothness indicators at $x_{i+1/2}$ by

$$\beta_k = |D_k^1 b_{i+1/2}| + |D_k^2 b_{i+1/2}| + |D_k^3 b_{i+1/2}|, \quad k = 0, 1, 2. \quad (3.2)$$

The Taylor expansion at $x_{i+1/2}$ of those smoothness indicators yields

$$\begin{aligned} \beta_0 &= \left| b'_{i+1/2} \Delta x + \frac{1}{24} b_{i+1/2}^{(4)} \Delta x^4 \right| + \left| b''_{i+1/2} \Delta x^2 - \frac{7}{24} b_{i+1/2}^{(4)} \Delta x^4 \right| + \left| b_{i+1/2}^{(3)} \Delta x^3 - b_{i+1/2}^{(4)} \Delta x^4 \right| + O(\Delta x^5), \\ \beta_1 &= \left| b'_{i+1/2} \Delta x - \frac{3}{640} b_{i+1/2}^{(5)} \Delta x^5 \right| + \left| b''_{i+1/2} \Delta x^2 + \frac{5}{24} b_{i+1/2}^{(4)} \Delta x^4 \right| + \left| b_{i+1/2}^{(3)} \Delta x^3 + \frac{1}{8} b_{i+1/2}^{(5)} \Delta x^5 \right| + O(\Delta x^6), \\ \beta_2 &= \left| b'_{i+1/2} \Delta x - \frac{1}{24} b_{i+1/2}^{(4)} \Delta x^4 \right| + \left| b''_{i+1/2} \Delta x^2 - \frac{7}{24} b_{i+1/2}^{(4)} \Delta x^4 \right| + \left| b_{i+1/2}^{(3)} \Delta x^3 + b_{i+1/2}^{(4)} \Delta x^4 \right| + O(\Delta x^5). \end{aligned}$$

Since β_0 and β_2 share the same components except the sign, we simply set

$$\tau_6 = |\beta_0 - \beta_2|,$$

the global smoothness indicator τ_6 on the stencil S^6 . Then the nonlinear positive and negative weights are defined by

$$\omega_k^\pm = \frac{\alpha_k^\pm}{\sum_{l=0}^2 \alpha_l^\pm}, \quad \alpha_k^\pm = \gamma_k^\pm \left(C + \left(\frac{\tau_6}{\beta_k + \epsilon} \right)^p \right), \quad k = 0, 1, 2, \quad (3.3)$$

with γ_k^\pm in (2.9) and $\epsilon = 10^{-40}$. We end up with the nonlinear weights

$$\omega_k = \sigma^+ \omega_k^+ - \sigma^- \omega_k^-,$$

as defined in (2.13).

Assuming that there is no critical point at $x_{i+1/2}$,

$$\tau_6 = D \left| b_{i+1/2}^{(4)} \right| \Delta x^4 + O(\Delta x^5),$$

with some constant $D > 0$. By the similar analysis as in Section 3.1, we obtain

$$\omega_k = d_k + O(\Delta x^{3p}).$$

In order to satisfy both conditions (2.14) and (2.15), the value of p is at least $4/3$. However, we have, by the Taylor expansion analysis again,

$$\omega_k = d_k + O(\Delta x^{2p}),$$

provided there exists a critical point at $x_{i+1/2}$, i.e., the first derivative is zero but the second derivative is not. For $p = 2$, the weight conditions are

$$\omega_0 - \omega_2 = O(\Delta x^4),$$

$$\omega_k - d_k = O(\Delta x^4),$$

which satisfy conditions (2.14) and (2.15) for the sixth order accuracy. Therefore, we set $p = 2$ for the proposed nonlinear weights as both conditions (2.14) and (2.15) are satisfied at the critical points. Since we want to see how the new smoothness indicators (3.2) affect the numerical solutions, C in (3.3) simply takes the value 1 in the numerical examples.

4 Numerical results

This section presents some numerical experiments to demonstrate the performance of proposed WENO schemes and compare with the WENO-LSZ scheme. We examine the accuracy of the WENO schemes for one- and two-dimensional heat equations in terms of L^1 , L^2 and L^∞ error norms:

$$\begin{aligned} L^1 &= \frac{1}{N+1} \sum_{i=0}^N |u_i(T) - u(x_i, T)|, \\ L^2 &= \sqrt{\frac{1}{N+1} \sum_{i=0}^N (u_i(T) - u(x_i, T))^2}, \\ L^\infty &= \max_{0 \leq i \leq N} |u_i(T) - u(x_i, T)|, \end{aligned}$$

where $u(x_i, T)$ denotes the exact solution and $u_i(T)$ is the numerical approximation at the final time $t = T$. The rest numerical experiments show the resolution of the numerical solutions with the WENO-LSZ and proposed WENO schemes. For time discretization, we use the explicit third-order total variation diminishing Runge-Kutta method [20]

$$\begin{aligned} u^{(1)} &= u^n + \Delta t L(u^n), \\ u^{(2)} &= \frac{3}{4} u^n + \frac{1}{4} u^{(1)} + \frac{1}{4} \Delta t L(u^{(1)}), \\ u^{n+1} &= \frac{1}{3} u^n + \frac{2}{3} u^{(2)} + \frac{2}{3} \Delta t L(u^{(2)}), \end{aligned}$$

where L is the spatial operator. We follow the CFL condition in [15] to set $\text{CFL} = 0.4$ unless otherwise stated. The WENO schemes in Section 3.1 and 3.2 are termed as WENO-DZ ($C = 10$, $p = 4/3$) and WENO-DS ($C = 1$, $p = 2$), respectively. We choose $\epsilon = 10^{-40}$ for both WENO-DZ and WENO-DS schemes whereas $\epsilon = 10^{-6}$ is kept for the WENO-LSZ scheme as in [15].

4.1 One-dimensional numerical examples

Example 4.1. We test the accuracy of those WENO schemes for the one-dimensional heat equation

$$u_t = u_{xx}, \quad -\pi \leq x \leq \pi, \quad t > 0$$

with the following initial data

$$u(x, 0) = \sin(x),$$

and the periodic boundary condition. The exact solution is given by

$$u(x, t) = e^{-t} \sin(x).$$

The numerical solution is computed up to the time $T = 2$ with the time step $\Delta t = \text{CFL} \cdot \Delta x^2$. We present the L_1, L_2 and L_∞ errors versus N , as well as the order of accuracy, for the WENO-LSZ, WENO-DZ, WENO-DS schemes in Tables 1, 2 and 3. It is clear that the expected order of accuracy is achieved for all schemes. Although the errors of the proposed schemes are larger than WENO-LSZ for small values of N , they are on the same scale as N increases.

Table 1: L_1 error and order of accuracy for Example 4.1.

N	WENO-LSZ		WENO-DZ		WENO-DS	
	Error	Order	Error	Order	Error	Order
10	6.32E-6	–	1.58E-5	–	1.73E-5	–
20	1.41E-7	5.4861	1.74E-7	6.5029	1.65E-7	6.7089
40	2.28E-9	5.9505	2.35E-9	6.2150	2.31E-9	6.1640
80	3.55E-11	6.0057	3.56E-11	6.0438	3.55E-11	6.0229
160	5.70E-13	5.9591	5.70E-13	5.9633	5.70E-13	5.9600

Table 2: L_2 error and order of accuracy for Example 4.1.

N	WENO-LSZ		WENO-DZ		WENO-DS	
	Error	Order	Error	Order	Error	Order
10	7.51E-6	–	1.90E-5	–	2.13E-5	–
20	1.61E-7	5.5402	2.00E-7	6.5703	1.91E-7	6.8003
40	2.57E-9	5.9732	2.64E-9	6.2421	2.60E-9	6.1973
80	3.97E-11	6.0163	3.98E-11	6.0545	3.97E-11	6.0347
160	6.35E-13	5.9641	6.35E-13	5.9683	6.35E-13	5.9651

Table 3: L_∞ error and order of accuracy for Example 4.1.

N	WENO-LSZ		WENO-DZ		WENO-DS	
	Error	Order	Error	Order	Error	Order
10	1.01E-5	–	2.67E-5	–	3.13E-5	–
20	2.31E-7	5.4485	2.89E-7	6.5295	2.85E-7	6.7788
40	3.67E-9	5.9770	3.78E-9	6.2567	3.74E-9	6.2494
80	5.64E-11	6.0241	5.66E-11	6.0618	5.65E-11	6.0506
160	9.02E-13	5.9684	9.02E-13	5.9722	9.01E-13	5.9699

Example 4.2. We then consider the PME (1.2). If the initial condition is set as the Dirac delta, the Barenblatt solution $B_m(x, t)$ [2, 22], representing the heat release from a point source,

takes the explicit formula

$$B_m(x, t) = t^{-q} \left[\left(1 - \frac{q(m-1)}{2m} \frac{x^2}{t^{2q}} \right)_+ \right]^{1/(m-1)}, \quad m > 1 \quad (4.1)$$

where $s_+ = \max(s, 0)$ and $q = (m+1)^{-1}$. For $t > 0$, the solution has a compact support $[-a_m(t), a_m(t)]$, where

$$\alpha_m(t) = \sqrt{\frac{2m}{k(m-1)}} t^k,$$

and the interfaces $|x| = a_m(t)$ move outward at a finite speed. Moreover, the larger the value of p , the sharper the interfaces that separate the compact support and the zero solution.

We begin with simulating the Barenblatt solution (4.1) of the PME (1.2) with the initial condition as the Barenblatt solution at $t = 1$, $u(x, 0) = B_m(x, 1)$, and the boundary conditions $u(\pm 6, t) = 0$ for $t > 0$. The final time is $T = 2$ and the time step is $\Delta t = \text{CFL} \cdot \Delta x^2 / m$. We take $N = 160$ and plot the numerical solutions at the final time for $m = 3, 5$ and 9 , in Figures 2, 3 and 4, respectively. We can see that the proposed WENO-DZ and WENO-DS give a sharper solution profile around the interfaces than WENO-LSZ. In Figure 2, there are some small-scale oscillations at $x = \pm 4.2$ introduced by WENO-LSZ, but those oscillations are smoothed by the proposed schemes.

We further look at how the numerical solution behaves with respect to the value of the constant C in (3.1) for WENO-DZ. We still take the example of the PME (1.2) for $m = 10$ together with the initial condition $u(x, 0) = B_{10}(x, 1)$ and the boundary conditions $u(\pm 6, t) = 0$ for $t > 0$, and plot the L_1, L_2 and L_∞ errors versus C in the interval $[1, 50]$ in Figure 5, given $N = 160$, $T = 2$ and $\Delta t = \text{CFL} \cdot \Delta x^2 / m$. This figure shows that the L_1 error grows while the L_2 and L_∞ errors decay as the value of C increases. In addition, the decay rates in L_2 and L_∞ errors, as well as the growth rate in L_1 error, are faster over $[1, 15]$ than the rest of the interval in C . Figure 6 shows the solution profiles with three different values of $C = 5, 10, 15$, where the numerical dissipation changes slightly around the sharp interfaces. Then a moderate value $C = 10$ is chosen for WENO-DZ in this paper.

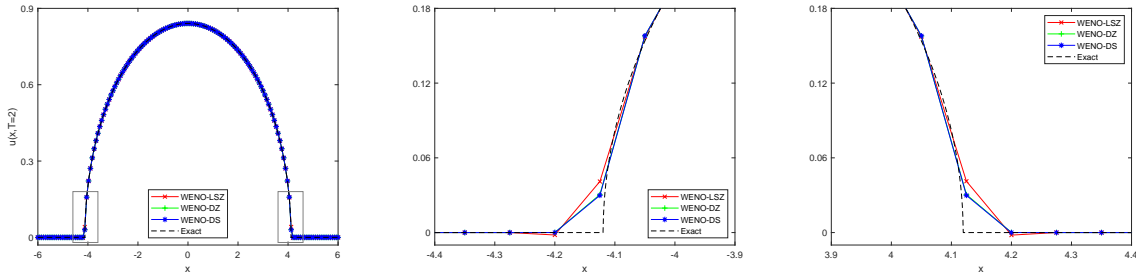


Figure 2: Barenblatt solution profiles for Example 4.2 with $m = 3$ at $T = 2$ (left), close-up view of the solutions in the boxes on the left/right (middle/right) computed by WENO-LSZ (red), WENO-DZ (green) and WENO-DS (blue) with $N = 160$. The dashed black lines are the exact solution.

Example 4.3. We continue to consider the PME (1.2), where the shape of the initial condition is two separate boxes. If the solution u represents the temperature, the PME models the variations in temperature when two hot spots are situated in the domain.

We first consider the PME with $m = 5$, where the initial condition is given by

$$u(x, 0) = \begin{cases} 1, & x \in (-3.7, -0.7) \cup (0.7, 3.7), \\ 0, & \text{otherwise,} \end{cases} \quad (4.2)$$

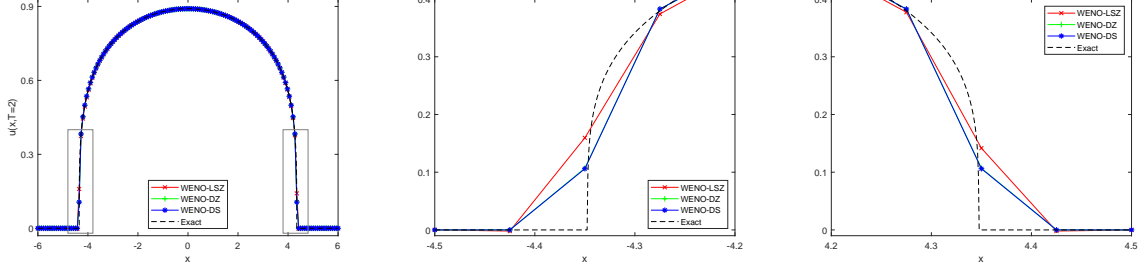


Figure 3: Barenblatt solution profiles for Example 4.2 with $m = 5$ at $T = 2$ (left), close-up view of the solutions in the boxes on the left/right (middle/right) computed by WENO-LSZ (red), WENO-DZ (green) and WENO-DS (blue) with $N = 160$. The dashed black lines are the exact solution.

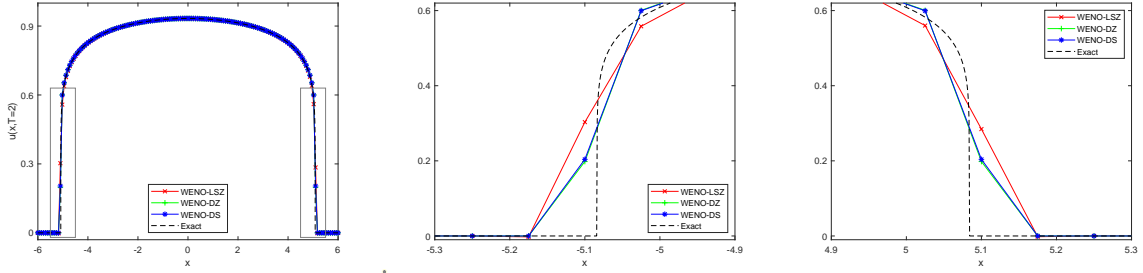


Figure 4: Barenblatt solution profiles for Example 4.2 with $m = 9$ at $T = 2$ (left), close-up view of the solutions in the boxes on the left/right (middle/right) computed by WENO-LSZ (red), WENO-DZ (green) and WENO-DS (blue) with $N = 160$. The dashed black lines are the exact solution.

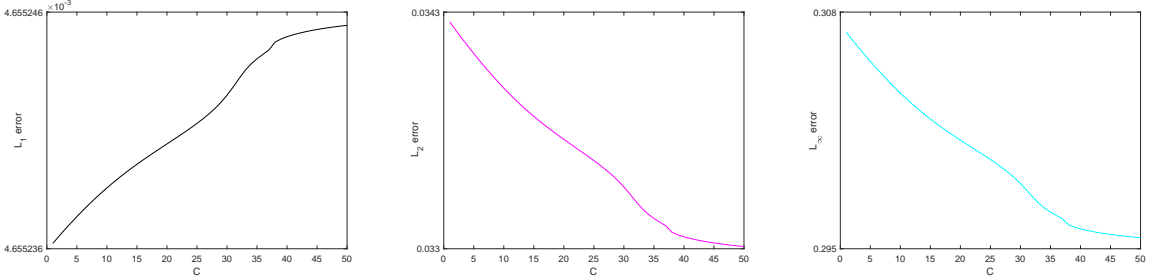


Figure 5: The L_1 (left), L_2 (middle) and L_∞ (right) errors of WENO-DZ versus C for Example 4.2 with $m = 10$ at $T = 2$.

in which the two boxes have the same height, and the boundary conditions are $u(\pm 5.5, t) = 0$ for $t > 0$. We divide the computational domain $[-5.5, 5.5]$ into $N = 220$ uniform cells. The final time is $T = 1.5$ and the time step is $\Delta t = \text{CFL} \cdot \Delta x^2 / m$. We present the numerical solutions at the final time, as shown in Figure 7.

Now we consider the PME with $m = 6$. The initial condition in this case is

$$u(x, 0) = \begin{cases} 1, & -4 < x < -1, \\ 2, & 0 < x < 3, \\ 0, & \text{otherwise,} \end{cases} \quad (4.3)$$

and the boundary conditions are $u(\pm 6, t) = 0$ for $t > 0$. We select $N = 240$ for the computational domain $[-6, 6]$. Figure 8 shows the approximate results obtained when solving PME up to the final time $T = 0.12$ with the time step $\Delta t = \text{CFL} \cdot \Delta x^2 / (m2^{m-1})$.

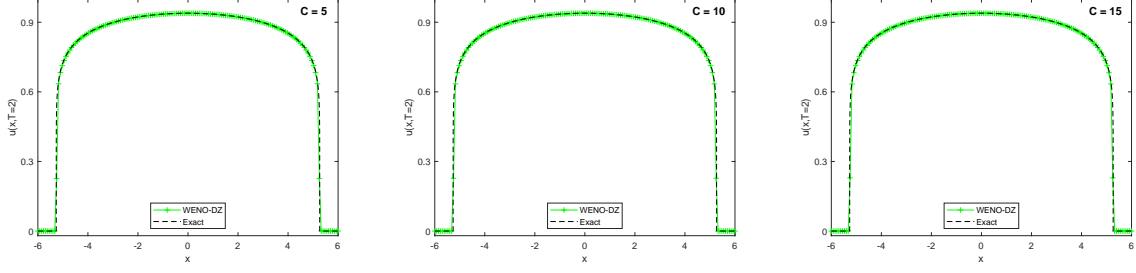


Figure 6: Barenblatt solution profiles for Example 4.2 with $m = 10$ at $T = 2$ computed by WENO-DZ with $C = 5$ (left), $C = 10$ (middle) and $C = 15$ (right). The dashed black lines are the exact solution.

As seen in Figures 7 and 8, all schemes are able to capture the sharp interfaces. However, the WENO-LSZ scheme produces small-scale oscillatory approximations around the sharp interfaces, whereas the proposed schemes exhibit non-oscillatory performance near those interfaces.

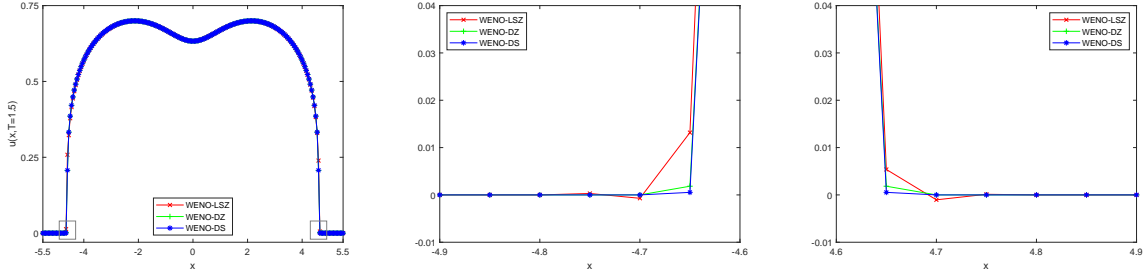


Figure 7: Solution profiles for PME (1.2) ($m = 5$) with the initial condition (4.2) at $T = 1.5$ (left), close-up view of the solutions in the boxes on the left/right (middle/right) approximated by WENO-LSZ (red), WENO-DZ (green) and WENO-DS (blue) with $N = 220$.

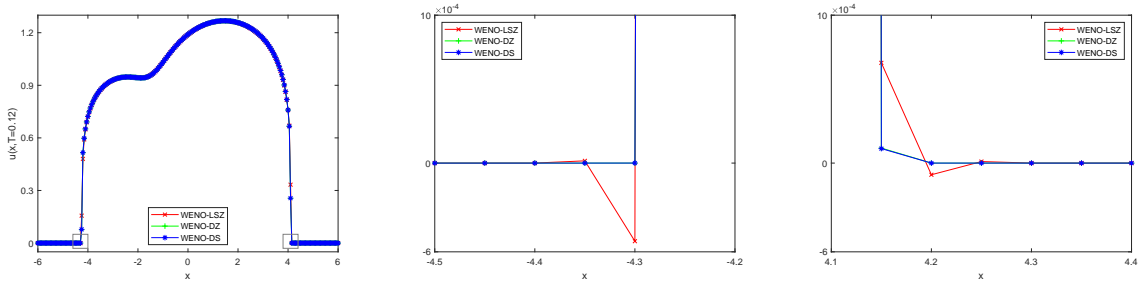


Figure 8: Solution profiles for PME (1.2) ($m = 6$) with the initial condition (4.3) at $T = 0.12$ (left), close-up view of the solutions in the boxes on the left/right (middle/right) approximated by WENO-LSZ (red), WENO-DZ (green) and WENO-DS (blue) with $N = 240$.

Next, we solve the one-dimensional scalar convection-diffusion equation of the form

$$u_t + f(u)_x = g(u)_{xx}.$$

Sometimes a source or sink term is added to the right-hand side. For the convection term, we use the fifth-order finite difference Lax–Friedrichs flux splitting WENO schemes: WENO-JS [11, 19] with WENO-LSZ, WENO-Z [3] with both WENO-DZ and WENO-DS. The numerical solution, computed by WENO-M [9] and WENO-LSZ for the respective convection and diffusion terms with a high resolution, will be referred to as the “exact” solution.

Example 4.4. The Buckley-Leverett equation [4] is of the form

$$u_t + f(u)_x = \epsilon(\nu(u)u_x)_x, \quad \epsilon\nu(u) \geq 0, \quad (4.4)$$

which is a prototype model for oil reservoir simulation. This is an example of degenerate parabolic equations since $\nu(u)$ vanishes at some values of u . Following [14], the convection flux $f(u)$ is of the s-shaped form

$$f(u) = \frac{u^2}{u^2 + (1-u)^2}, \quad (4.5)$$

$\epsilon = 0.01$, and

$$\nu(u) = \begin{cases} 4u(1-u), & 0 \leq u \leq 1, \\ 0, & \text{otherwise.} \end{cases} \quad (4.6)$$

The diffusion term $\epsilon(\nu(u)u_x)_x$ can be written in the form of $g(u)_{xx}$, where

$$g(u) = \begin{cases} 0, & u < 0, \\ \epsilon\left(-\frac{4}{3}u^3 + 2u^2\right), & 0 \leq u \leq 1, \\ \frac{2}{3}\epsilon, & u > 1. \end{cases}$$

The initial condition is given by

$$u(x, 0) = \begin{cases} 1 - 3x, & 0 \leq x \leq 1/3, \\ 0, & 1/3 < x \leq 1. \end{cases}$$

and the Dirichlet boundary condition is $u(0, t) = 1$. The computational domain $[0, 1]$ is divided into $N = 100$ uniform cells and the time step is $\Delta t = \text{CFL} \cdot \Delta x^2$. The numerical solutions computed by those WENO schemes at $T = 0.2$ are presented in Figure 9, with WENO-DZ and WENO-DS being more accurate than WENO-LSZ.

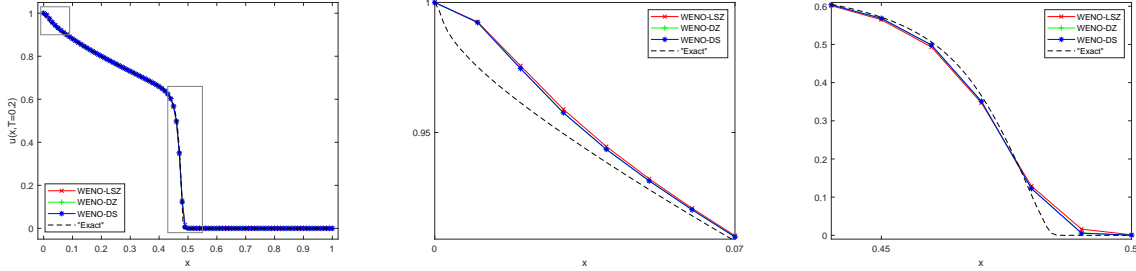


Figure 9: Solution profiles for Buckley-Leverett equation in Example 4.4 at $T = 0.2$ (left), close-up view of the solutions in the boxes on the left/right (middle/right) computed by WENO-LSZ (red), WENO-DZ (green) and WENO-DS (blue) with $N = 100$. The dashed black lines are generated by WENO-M and WENO-LSZ with $N = 1000$.

Example 4.5. We continue to consider the Buckley-Leverett equation (4.4) with the same $\epsilon = 0.01$ and $\nu(u)$ (4.6) as in Example 4.4. The flux function $f(u)$ with gravitational effects is

$$f(u) = \frac{u^2}{u^2 + (1-u)^2}(1 - 5(1-u)^2), \quad (4.7)$$

where the sign of $f'(u)$ changes in $[0, 1]$. The Riemann initial condition is

$$u(x, 0) = \begin{cases} 0, & 0 \leq x < 1 - 1/\sqrt{2}, \\ 1, & 1 - 1/\sqrt{2} \leq x \leq 1. \end{cases}$$

We divide the computational domain $[0, 1]$ into $N = 100$ uniform cells and the time step is $\Delta t = \text{CFL} \cdot \Delta x^2$. Figure 10 shows the numerical solutions at $T = 0.2$ for the convection flux $f(u)$ (4.7) with gravitational effects while Figure 11 presents the ones for $f(u)$ (4.5) without gravitational effects. Zooming in the right boxes in both Figures 10 and 11 shows clearly that WENO-DZ and WENO-DS produce more accurate numerical solutions than WENO-LSZ. However, for the numerical solutions in the left boxes, WENO-DZ and WENO-DS give more sharper results around the transitions than WENO-LSZ.

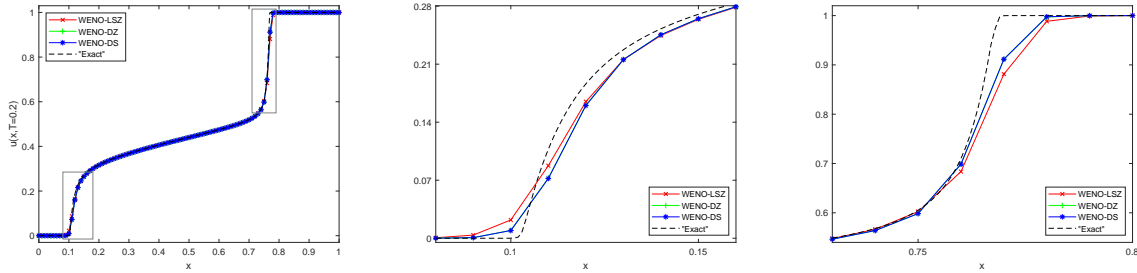


Figure 10: Solution profiles for Buckley-Leverett equation (4.4) with gravitation in Example 4.5 at $T = 0.2$ (left), close-up view of the solutions in the boxes on the left/right (middle/right) computed by WENO-LSZ (red), WENO-DZ (green) and WENO-DS (blue) with $N = 100$. The dashed black lines are generated by WENO-M and WENO-LSZ with $N = 1000$.

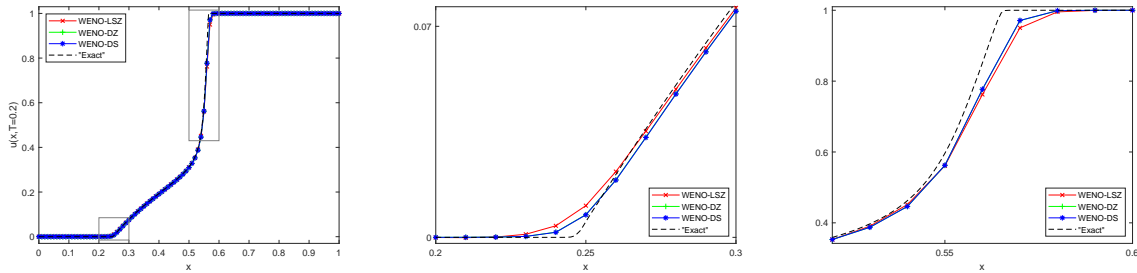


Figure 11: Solution profiles for Buckley-Leverett equation (4.4) without gravitation in Example 4.5 at $T = 0.2$ (left), close-up view of the solutions in the boxes on the left/right (middle/right) computed by WENO-LSZ (red), WENO-DZ (green) and WENO-DS (blue) with $N = 100$. The dashed black lines are generated by WENO-M and WENO-LSZ with $N = 1000$.

Example 4.6. In this example, we consider the strongly degenerate parabolic convection-diffusion equation

$$u_t + f(u)_x = \epsilon(\nu(u)u_x)_x, \quad \epsilon\nu(u) \geq 0. \quad (4.8)$$

We take $\epsilon = 0.1$, $f(u) = u^2$, and

$$\nu(u) = \begin{cases} 0, & |u| \leq 0.25, \\ 1, & |u| > 0.25. \end{cases} \quad (4.9)$$

If $|u| \leq 0.25$, the equation (4.8) returns to the hyperbolic equation. The diffusion term $\epsilon(\nu(u)u_x)_x$ can be written in the form of $g(u)_{xx}$, where

$$g(u) = \begin{cases} \epsilon(u + 0.25), & u < -0.25, \\ \epsilon(u - 0.25), & u > 0.25, \\ 0, & \text{otherwise.} \end{cases}$$

The initial condition is given by

$$u(x, 0) = \begin{cases} 1, & -1/\sqrt{2} - 0.4 < x < -1/\sqrt{2} + 0.4, \\ -1, & 1/\sqrt{2} - 0.4 < x < 1/\sqrt{2} + 0.4, \\ 0, & \text{otherwise.} \end{cases}$$

We divide the computational domain $[-2, 2]$ into $N = 200$ uniform cells and the time step is $\Delta t = \text{CFL} \cdot \Delta x^2$. The numerical simulations at $T = 0.7$ are presented in Figure 12, where WENO-DZ and WENO-DS show more accurate results than WENO-LSZ.

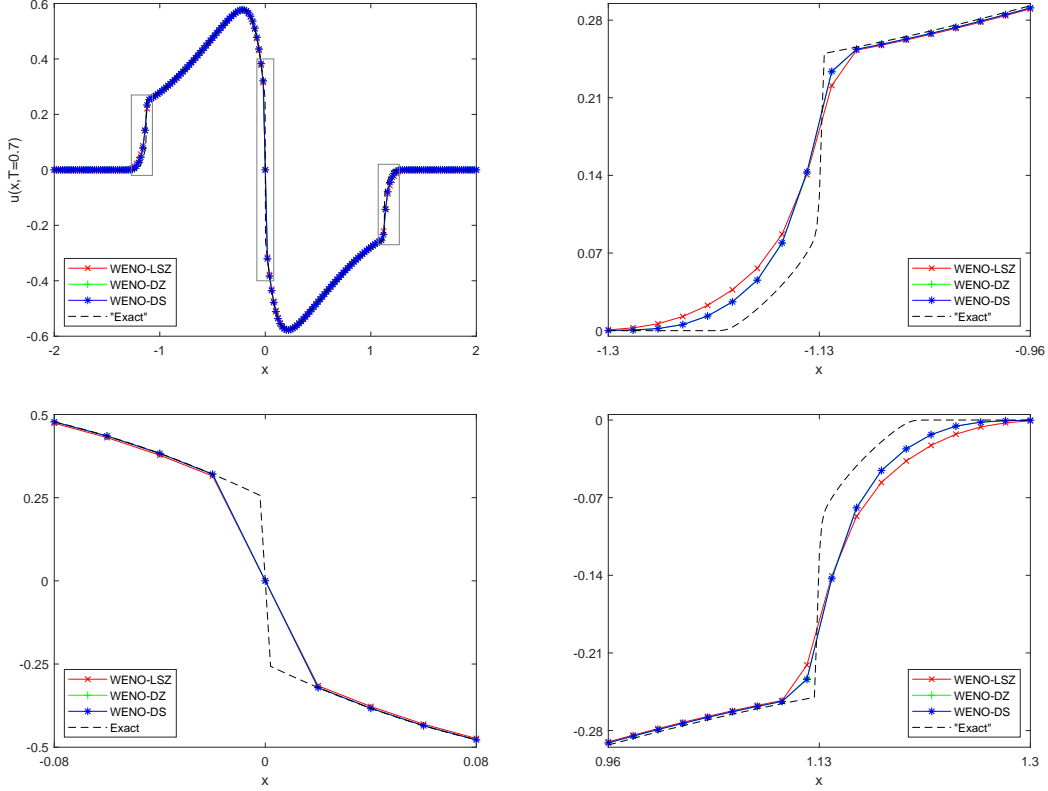


Figure 12: Solution profiles for Example 4.6 at $T = 0.7$ (top left), close-up view of the solutions in the boxes on the left/middle/right (top right/bottom left/bottom right) computed by WENO-LSZ (red), WENO-DZ (green) and WENO-DS (blue) with $N = 200$. The dashed black lines are generated by WENO-M and WENO-LSZ with $N = 2000$.

Example 4.7. Now we consider the glacier growth model [5, 13],

$$h_t + f(h)_x = \epsilon (\nu(h)h_x)_x + S(x, t, h),$$

where $h(x, t)$ is the height of a glacier resting upon a flat mountain and a source term $S(x, t, h)$ is added to the equation. Following [14] again, we set $\epsilon = 0.01$, $f(h) = \frac{h+3h^6}{4}$ and $\nu(h) = 3h^6$. The diffusion term $\epsilon (\nu(h)h_x)_x$ can be written as $g(h)_{xx}$ with $g(h) = \frac{3}{7}\epsilon h^7$. The Riemann initial condition,

$$h(x, 0) = \begin{cases} 1, & x < 0, \\ 0, & x > 0, \end{cases}$$

describes the outlet into a valley neglecting seasonal variations. Let

$$S_0(x) = \begin{cases} 0, & x < -0.4, \\ (x + 0.4)/2, & -0.4 \leq x \leq -0.2, \\ -x/2, & x > -0.2. \end{cases}$$

The source term is given by

$$S(x, t, h) = \begin{cases} S_0(x), & h(x, t) > 0, \\ \max(S_0(x), 0), & h(x, t) = 0. \end{cases}$$

The computational domain $[-0.5, 2.5]$ is divided into $N = 100$ uniform cells and the time step is $\Delta t = \text{CFL} \cdot \Delta x^2$. We approximate the solutions up to $T = 2$, as shown in Figure 13. Although the numerical solutions computed by WENO-DZ and WENO-DS are closer to the reference solution than WENO-LSZ, there is clearly room for improvement in the WENO approach to the glacier growth model.

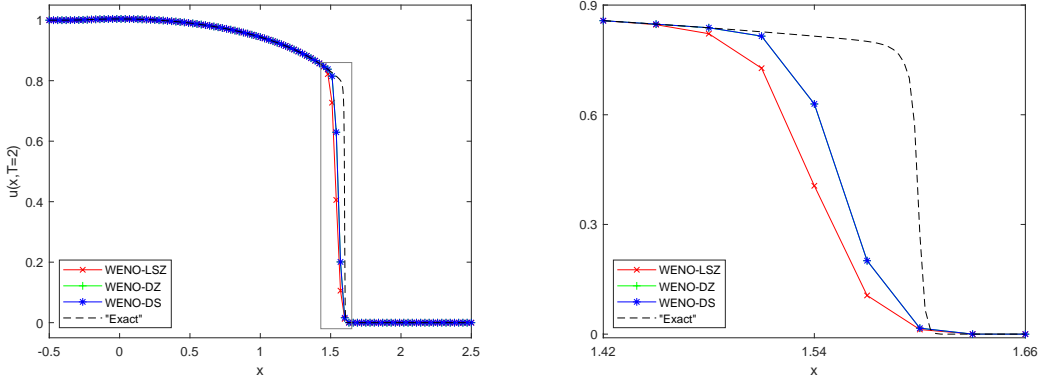


Figure 13: Solution profiles for Example 4.7 at $T = 2$ (left), close-up view of the solutions in the box (right) computed by WENO-LSZ (red), WENO-DZ (green) and WENO-DS (blue) with $N = 100$. The dashed black lines are generated by WENO-M and WENO-LSZ with $N = 1000$.

4.2 Two-dimensional numerical examples

Example 4.8. We test the accuracy of those WENO schemes for the two-dimensional heat equation

$$u_t = u_{xx} + u_{yy}, \quad -\pi \leq x, y \leq \pi, \quad t > 0 \quad (4.10)$$

subject to the initial data

$$u(x, y, 0) = \sin(x + y),$$

and the periodic boundary conditions in both directions. The exact solution is

$$u(x, t) = e^{-2t} \sin(x + y).$$

The numerical solutions are computed at the final time $T = 2$ with the time step $\Delta t = 0.2 \cdot \min(\Delta x, \Delta y)^2$. The L_1 , L_2 , and L_∞ errors, along with the orders of accuracy, are provided in Tables 4, 5 and 6, respectively. All WENO schemes exhibit sixth order accuracy. As in Examples 4.1, the errors of proposed schemes are larger than WENO-LSZ for small values of N , and they converge as N increases.

Example 4.9. Consider the two-dimensional PME given by

$$u_t = (u^2)_{xx} + (u^2)_{yy},$$

with the initial condition

$$u(x, y, 0) = \begin{cases} \exp\left(-\frac{1}{6-(x-2)^2-(y+2)^2}\right), & (x-2)^2 + (y+2)^2 < 6, \\ \exp\left(-\frac{1}{6-(x+2)^2-(y-2)^2}\right), & (x+2)^2 + (y-2)^2 < 6, \\ 0, & \text{otherwise,} \end{cases}$$

Table 4: L_1 errors and order of convergence for Example 4.8.

N	WENO-LSZ		WENO-DZ		WENO-DS	
	Error	Order	Error	Order	Error	Order
10×10	1.85E-6	–	4.61E-6	–	5.10E-6	–
20×20	4.06E-8	5.5104	4.93E-8	6.5473	4.69E-8	6.7642
40×40	6.33E-10	6.0025	6.50E-10	6.2443	6.39E-10	6.1962
80×80	9.72E-12	6.0265	9.74E-12	6.0598	9.72E-12	6.0394
160×160	1.55E-13	5.9675	1.55E-13	5.9712	1.55E-13	5.9680

Table 5: L_2 errors and order of convergence for Example 4.8.

N	WENO-LSZ		WENO-DZ		WENO-DS	
	Error	Order	Error	Order	Error	Order
10×10	2.12E-6	–	5.31E-6	–	5.93E-6	–
20×20	4.55E-8	5.5423	5.53E-8	6.5869	5.27E-8	6.8143
40×40	7.05E-10	6.0113	7.24E-10	6.2548	7.12E-10	6.2098
80×80	1.08E-11	6.0291	1.08E-11	6.0622	1.08E-11	6.0423
160×160	1.72E-13	5.9681	1.73E-13	5.9717	1.72E-13	5.9687

Table 6: L_∞ errors and order of convergence for Example 4.8.

N	WENO-LSZ		WENO-DZ		WENO-DS	
	Error	Order	Error	Order	Error	Order
10×10	2.80E-6	–	7.16E-6	–	8.18E-6	–
20×20	6.42E-8	5.4484	7.81E-8	6.5180	7.57E-8	6.7550
40×40	9.98E-10	6.0077	1.02E-9	6.2547	1.01E-9	6.2284
80×80	1.53E-11	6.0294	1.53E-11	6.0617	1.53E-11	6.0462
160×160	2.44E-13	5.9681	2.44E-13	5.9716	2.44E-13	5.9691

and the periodic boundary condition in each direction. We divide the square computational domain $[-10, 10] \times [-10, 10]$ into $N_x \times N_y = 80 \times 80$ uniform cells and the time step $\Delta t = \text{CFL} \cdot \min(\Delta x, \Delta y)^4 / 2$. The numerical solutions at $T = 1$ and $T = 4$ are shown in Figures 14 and 15, respectively. At the time $T = 1$, there are some small-scale oscillations around the free boundaries in the solution by WENO-LSZ, which are implied by the white spots in the surface plot on the top left of Figure 14. The amplitude of the oscillations decrease by WENO-DS, but the white spots are evident in the surface plot on the top right. The oscillations are largely damped by WENO-DZ as there is no obvious white spot in the surface plot on the top middle. However, at the time $T = 4$, all WENO schemes are able to capture the free boundaries without noticeable oscillation, as shown in Figure 15.

Example 4.10. We consider the two-dimensional Buckley-Leverett equation of the form

$$u_t + f_1(u)_x + f_2(u)_y = \epsilon (u_{xx} + u_{yy}),$$

with $\epsilon = 0.01$ and the flux functions given by

$$f_1(u) = \frac{u^2}{u^2 + (1-u)^2}, \quad f_2(u) = (1 - 5(1-u)^2) f_1(u).$$

Then the equation includes gravitational effects only in the y-direction. The initial condition is

$$u(x, y, 0) = \begin{cases} 1, & x^2 + y^2 < 0.5, \\ 0, & \text{otherwise.} \end{cases}$$

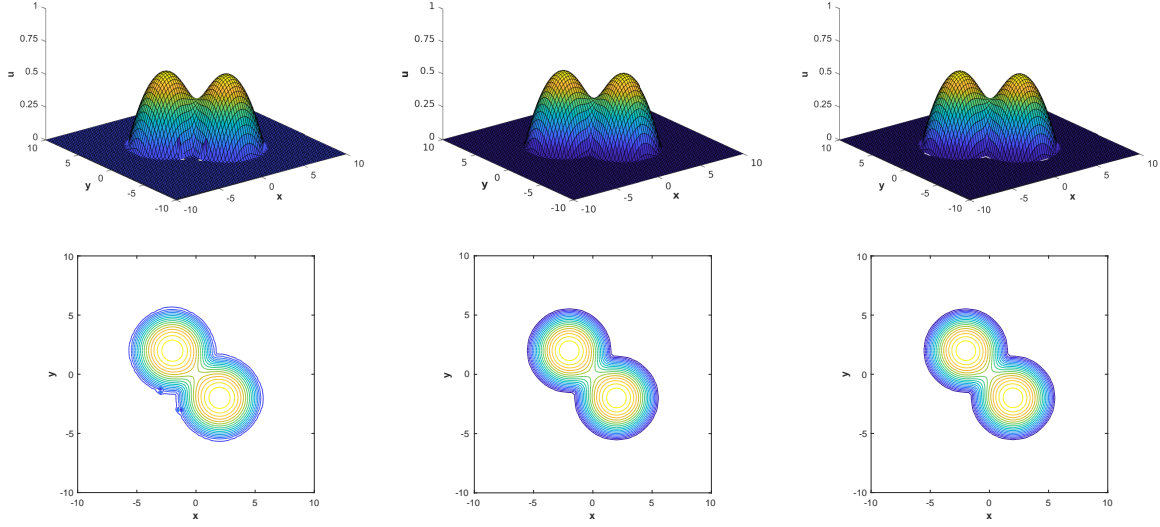


Figure 14: Solutions in the surface (top) and contour (bottom) plots for Example 4.9 at $T = 1$ by WENO-LSZ (left), WENO-DZ (middle) and WENO-DS (right) with $N_x \times N_y = 80 \times 80$. Each contour plot includes 18 contours of u .

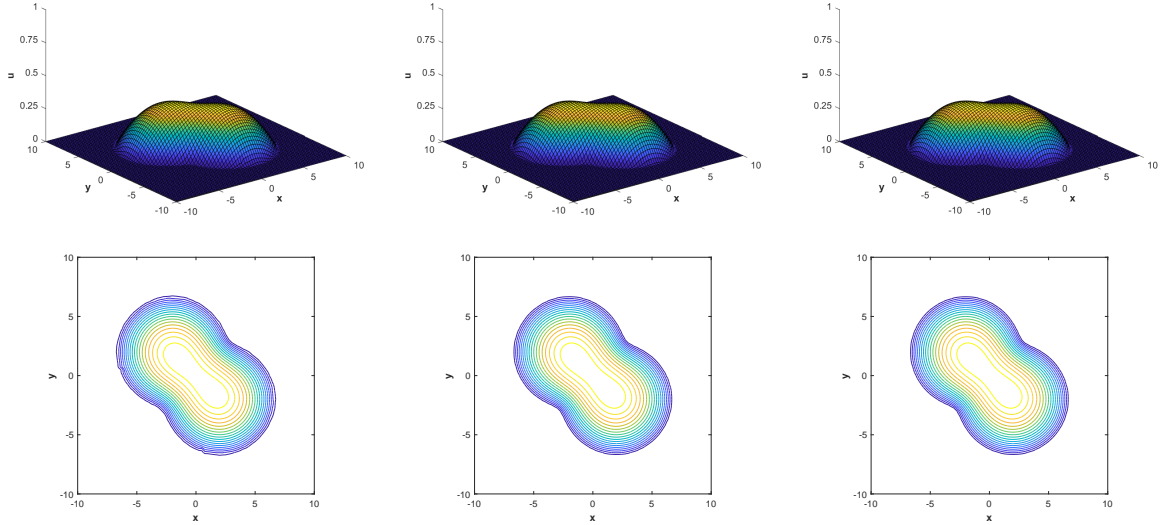


Figure 15: Solutions in the surface (top) and contour (bottom) plots for Example 4.9 at $T = 4$ by WENO-LSZ (left), WENO-DZ (middle) and WENO-DS (right) with $N_x \times N_y = 80 \times 80$. Each contour plot includes 18 contours of u .

The square computational domain $[-1.5, 1.5] \times [-1.5, 1.5]$ is divided into $N_x \times N_y = 120 \times 120$ uniform cells and the time step is $\Delta t = \text{CFL} \cdot \min(\Delta x, \Delta y)^2$. All WENO schemes yield similar numerical results at $T = 0.5$, as shown in Figure 16.

Example 4.11. We conclude this section with the two-dimensional strongly degenerate parabolic convection-diffusion equation

$$u_t + f(u)_x + f(u)_y = \epsilon (\nu(u)u_x)_x + \epsilon (\nu(u)u_y)_y,$$

where $\epsilon = 0.1$, $f(u) = u^2$, and $\nu(u)$ (4.9) are the same as in Example 4.6. The initial condition

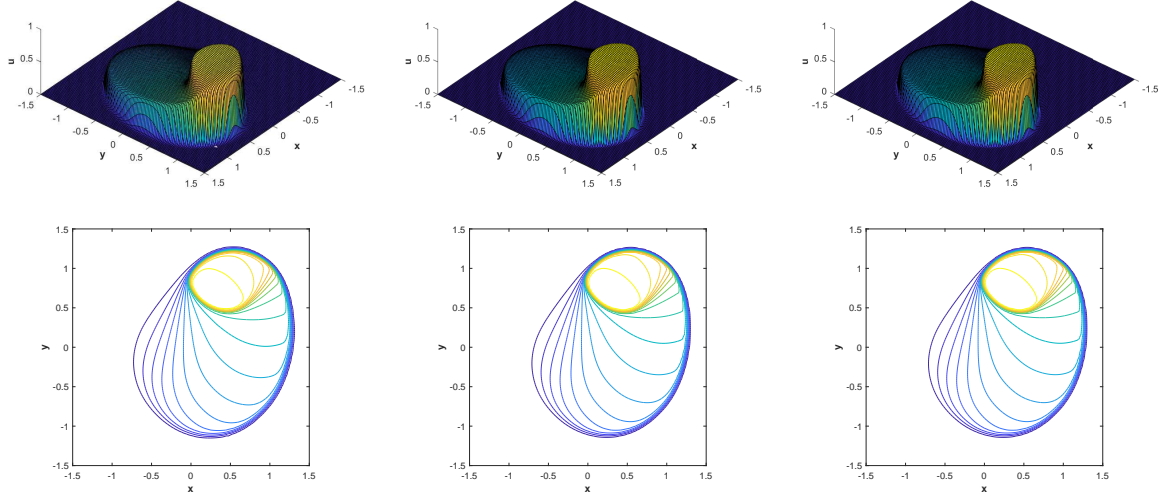


Figure 16: Solutions in the surface (top) and contour (bottom) plots for Example 4.10 at $T = 0.5$ by WENO-LSZ (left), WENO-DZ (middle) and WENO-DS (right) with $N_x \times N_y = 120 \times 120$. Each contour plot includes 18 contours of u .

is

$$u(x, y, 0) = \begin{cases} 1, & (x + 0.5)^2 + (y + 0.5)^2 < 0.16, \\ -1, & (x - 0.5)^2 + (y - 0.5)^2 < 0.16, \\ 0, & \text{otherwise.} \end{cases}$$

We divide the computational domain $[-1.5, 1.5] \times [-1.5, 1.5]$ into $N_x \times N_y = 120 \times 120$ uniform cells and the time step is $\Delta t = \text{CFL} \cdot \min(\Delta x, \Delta y)^2$. The numerical solutions at $T = 0.5$, generated by those WENO schemes, look similar in Figure 17.

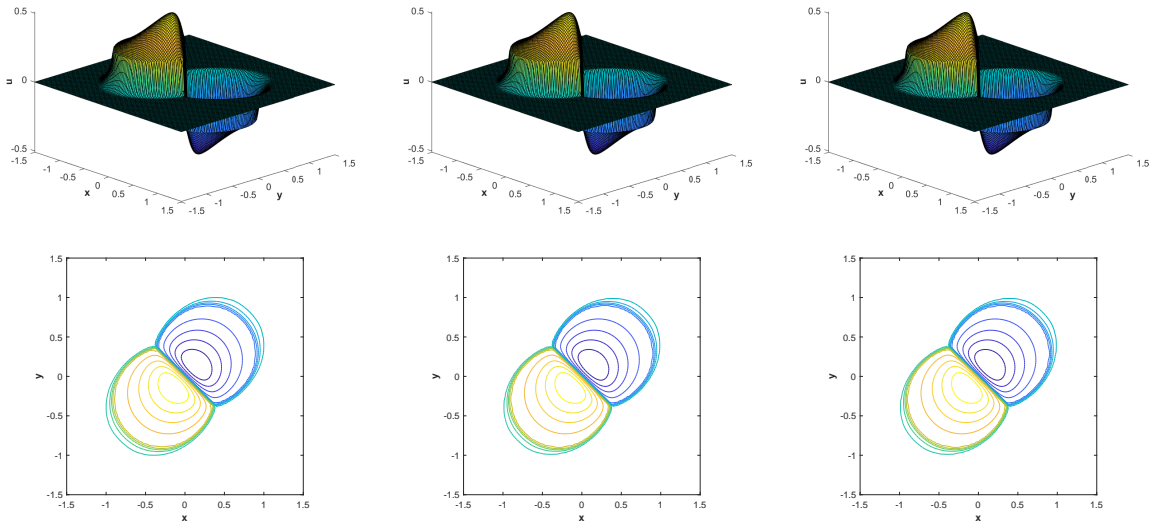


Figure 17: Solutions in the surface (top) and contour (bottom) plots for Example 4.11 at $T = 0.5$ by WENO-LSZ (left), WENO-DZ (middle) and WENO-DS (right) with $N_x \times N_y = 120 \times 120$. Each contour plot includes 18 contours of u .

5 Conclusion

In this paper, we propose two kinds of Z-type nonlinear weights of sixth order finite difference WENO schemes for approximating nonlinear degenerate parabolic equations: one is the generalization of MWENO weights [6] and the other one is based on the generalized undivided difference. Numerical examples show that the proposed WENO schemes achieve the sixth order accuracy and inhibit the small-scale oscillations introduced by the WENO-LSZ scheme [15].

Acknowledgments

The first author is supported by Samsung Science & Technology Foundation under the grant number SSTF-BA1802-02 and the second author is supported by IIPE, Visakhapatnam, India, under the IRG grant number IIPE/DORD/IRG/001.

References

- [1] D. G. Aronson, The porous medium equation, in *Nonlinear Diffusion Problems*, edited by A. Fasano, and M. Primicerio, Lecture Notes in Mathematics, (Springer-Verlag, Berlin/New York, 1986), pp. 1–46.
- [2] G. I. Barenblatt, On self-similar motions of compressible fluid in a porous medium, *Prikl. Mat. Mekh.* 16 (1952) 679–698 (in Russian).
- [3] R. Borges, M. Carmona, B. Costa, W.S. Don, An improved weighted essentially non-oscillatory scheme for hyperbolic conservation laws, *J. Comput. Phys.* 227 (2008) 3191–3211.
- [4] S. E. Buckley, M. C. Leverett, Mechanism of fluid displacement in sands, *Trans. AIME.* 146 (1942) 107–116.
- [5] A. C. Fowler, Glaciers and ice sheets, in *The Mathematics of Models for Climatology and Environment*, edited by J. I. Díaz, NATO ASI Series, (Springer, Berlin, Heidelberg, 1997), pp. 301–336.
- [6] M. Hajipour, A. Malek, High accurate NRK and MWENO scheme for nonlinear degenerate parabolic PDEs, *Appl. Math. Modell.* 36 (2012) 4439–4451.
- [7] Y. Ha, C. H. Kim, Y. J. Lee, J. Yoon, An improved weighted essentially non-oscillatory scheme with a new smoothness indicator, *J. Comput. Phys.* 232 (2013) 68–86.
- [8] Y. Ha, C. H. Kim, Y. H. Yang, J. Yoon, Sixth-order weighted essentially nonoscillatory schemes based on exponential polynomials, *SIAM J. Sci. Comput.* 38 (2016) A1987–A2017.
- [9] A. K. Henrick, T. D. Aslam, J. M. Powers, Mapped weighted essentially non-oscillatory schemes: achieving optimal order near critical points, *J. Comput. Phys.* 207 (2005) 542–567.
- [10] X. Y. Hu, Q. Wang, N. A. Adams, An adaptive central-upwind weighted essentially non-oscillatory scheme, *J. Comput. Phys.* 229 (2010) 8952–8965.
- [11] G.-S Jiang, C.-W. Shu, Efficient implementation of weighted ENO schemes, *J. Comput. Phys.* 126 (1996) 202–228.
- [12] Y. Jiang, High order finite difference multi-resolution WENO method for nonlinear degenerate parabolic equations, *J. Sci. Comput.* 86 (2021). <https://doi.org/10.1007/s10915-020-01382-y>

- [13] K. H. Karlsen, K. A. Lie, An unconditionally stable splitting for a class of nonlinear parabolic equations, *IMA J. Numer. Anal.* 19 (1999) 609–635.
- [14] A. Kurganov, E. Tadmor, New high-resolution central schemes for nonlinear conservation laws and convection-diffusion equations, *J. Comput. Phys.* 160 (2000) 241–282.
- [15] Y. Liu, C.-W. Shu, M. Zhang, High order finite difference WENO schemes for nonlinear degenerate parabolic equations, *SIAM J. Sci. Comput.* 33 (2011) 939–965.
- [16] M. Muskat, *The flow of homogeneous fluids through porous media*, McGraw-Hill, New York, 1937.
- [17] S. Rathan, R. Kumar, A. D. Jagtap, L^1 -type smoothness indicators based WENO scheme for nonlinear degenerate parabolic equations, *Appl. Math. Comput.* 375 (2020) 125112. <https://doi.org/10.1016/j.amc.2020.125112>
- [18] J. Shi, C. Hu, C.-W. Shu, A technique of treating negative weights in WENO schemes, *J. Comput. Phys.* 175 (2002) 108–127.
- [19] C.-W. Shu, Essentially non-oscillatory and weighted essentially non-oscillatory schemes for hyperbolic conservation laws, in *Advanced Numerical Approximation of Nonlinear Hyperbolic Equations*, edited by B. Cockburn, C. Johnson, C.-W. Shu, and E. Tadmor, *Lecture Notes in Mathematics*, (Springer-Verlag, Berlin/New York, 1998), pp. 325–432.
- [20] C.-W. Shu, S. Osher, Efficient implementation of essentially non-oscillatory shock capturing schemes, *J. Comput. Phys.* 77 (1988) 439–471.
- [21] J. L. Vázquez, The interfaces of one-dimensional flows in porous media, *Trans. Amer. Math. Soc.* 285 (1984) 717–737.
- [22] Ya. B. Zel’dovich, A. S. Kompaneetz, Towards a theory of heat conduction with thermal conductivity depending on the temperature, in *Collection of Papers Dedicated to 70th Birthday of Academician A.F. Ioffe*, (Izd. Akad. Nauk SSSR, Moscow, 1950), pp. 61–72.
- [23] Ya. B. Zel’dovich, Yu. P. Raizer, *Physics of shock waves and high-temperature hydrodynamic phenomena*, Academic Press, New York, 1966.